Int J Adv Manuf Technol (2006) 30: 10–19
DOI 10.1007/s00170-005-0032-y

ORIGINAL ARTICLE

Jenq-Shyong Chen · Yii-Wen Hwang

Centrifugal force induced dynamics of a motorized high-speed spindle

Received: 26 November 2004 / Accepted: 11 March 2005 / Published online: 12 October 2005

Abstract Trend of the high-speed and high efficiency machining has pushed the continuous demand of higher spindle speed and power for the machining center application. Because the extremely high speed produces significant centrifugal force, it creates a need to predict the spindle dynamical characteristics at dynamic states. This work presents analysis results of the spindle dynamic of a motorized high speed spindle with angular ball contact bearings. For a machining center, two major subsystems determining the overall spindle stiffness are the shaft/bearing subsystem and the draw bar mechanism subsystem. Shaft/bearing stiffness as well as the natural frequency decreased at high speeds due to the bearing softening and gyroscopic effect. The bearing softening is the major reason of the reduced spindle stiffness, while the gyroscopic effect plays the secondary effect. Angular contact ball bearing softening at high speed is due to the reduced contact load and increased contact angle at the ball/inner-raceway contact interface caused by the centrifugal force. For the draw bar mechanism, analysis results show that the dynamic draw force at high speeds is significantly increased from that designed at the static state. Because the toolholder/spindle interface stiffness is proportional to the draw force, centrifugal force theoretically contributes a plus to the spindle stiffness at dynamic state. The dynamic draw force, however, is dependent on the friction loss inside the draw bar mechanism. Because of the low friction coefficient, the ball-type mechanism is superior to the wedge type mechanism.

Keywords Bearing · Centrifugal force · Draw bar mechanism · High-speed spindle · Spindle dynamics

J.-S. Chen (✉) · Y.-W. Hwang
Department of Mechanical Engineering,
National Chung-Cheng University,
160, San-Hsing, Ming-Hsiung,
Chia-Yi, 621, Taiwan
e-mail: imejsc@ccu.edu.tw
Tel.: +886-5-2720588
Fax: +886-5-2720589

1 Introduction

High-speed cutting technology is now being used increasingly in a broad range of applications to machine ferrous metals and nonmetallic materials. The angular contact ball bearing spindle with integrated induction motor between front and rear bearings [1–2] is the most popular spindle type for these applications. A widely adopted measure of high speed effects in bearings is the DN or DmN value (bearing bore diameter D/mm or bearing pitch diameter Dm/mm multiplied by shaft speed N/rpm). In particular applications such as high-speed aluminum cutting for the aircraft structures, DN value has reached 2–3 million, and is expected to require bearings to operate with DN as high as 3.5–4 million. As reported in a work [3], today's state of the art of spindle technology does not reach the allowable cutting speeds and material removal rates of aluminum, copper alloys, and composites. Therefore, trend of the high-speed and high efficiency machining has continuously pushed the demand of higher spindle speed and power for the machining center application. It, therefore, creates the need to predict the centrifugal force induced spindle dynamics at high speeds.

For a machining center, two major subsystems determining the overall spindle stiffness are the shaft/bearing subsystem and the draw bar mechanism subsystem. Shaft/bearing stiffness is decided by the bearing type, layout, preload and interference, while the draw bar mechanism stiffness is decided by the draw force and the spindle/toolholder junction interface. Early studies on spindle systems stiffness mainly dealt with static models, calculating stiffness with applied static loads. The main focus of these activities was to determine the optimum bearing span, bearing preload, draw bar force, and toolhoder interface [4–9] at the static state.

Tlusty et al. [10] proved both in computationally and experimentally that roller bearings have the characteristics of "softening" spring when the static bearing preload exceeds a determined level. Later, Soon and Stone [11] developed a shaft/bearing model considering the bearing

nonlinear effects. These two works, however, only considered the static-load-induced nonlinear characteristics of the bearings. Shin [12] found that at high speeds, centrifugal force loading in the bearing causes stiffness softening, creating a change in natural frequency. Stein and Tu [13] developed a thermo-elastic model for determining transient and steady state thermally-induced bearing loads. They found the thermally-induced bearing load plays an important role to the bearing life and spindle dynamic characteristics at the high rotating speed. Later, comprehensive models of integrated thermal, mechanical, and dynamical characteristics of the high-speed spindle have been developed [14–15] to predict the bearing load and spindle dynamics changed at high rotating speed.

For a machining center, a draw bar mechanism is designed inside the spindle shaft in order to allow automatic tool exchange for different cutting conditions. A draw bar mechanism consists of a pull-in mechanism and a tapered toolholder/spindle interface. The toolholder/spindle interface stiffness plays an important role to the overall machine stiffness. Riven [16] found that the weakest link in the machining system is the toolholder/spindle interface using the conventional 7/24 tapered toolholder. It was found that 25–50% of the tool end deformation was due to the 7/24 taper toolholder/spindle connection. The rigidity of the toolholder/spindle connection had been improved by the later development of the HSK tool interface [11]. Aoyama and Inasaki [17] found, through numerical analysis and experimental tests, that when the spindle rotates at high speed, the radial stiffness of the HSK tool interface decreases with increasing spindle speed due to the loss contact at the tapered face in the high-speed range. The spindle bore and the components of the HSK tool interface elastically expand due to the increase centrifugal force, and the contact at the tapered face consequently becomes loose.

The toolholder/spindle interface stiffness is determined by the tapered interface clearance. In general, increasing the draw force will usually yield larger contact area and consequently better contact stiffness of the toolholder/spindle interface. However, the slope of increased contact stiffness becomes flattened when the draw force reaches a certain level. For example, the contact stiffness of a SK50 tool holder was not much improved when the draw force was beyond 20KN [18]. On the contrary, it was also reported that while increasing the draw force leads to greater static stiffness in the tool-spindle interface, dynamic measurements indicate that higher draw forces also diminish the interface damping [19].

High draw bar force is demanded to ensure a guaranteed tool/spindle interface clearance. For example, 9–25 kN is required for the SK-50 toolholder [16]. The draw force of a draw bar mechanism is usually produced through the stacked disc springs. In order to produce a compact draw mechanism inside the spindle shaft, the disc-spring force is, often, magnified by a force amplification mechanism consisting of either a ball type or wedge type mechanism. Benefits from the force amplification mechanism include compactness, better fatigue life, and better mass balance of the stacked disc springs. One problem regarding the conventional draw bar mechanism is that the disc spring and force amplification mechanism are designed based on the static load analysis. Little attention has been put on the dynamic characteristics of the draw bar mechanism at dynamic state. Another problem is that the mechanical efficiency of the draw bar mechanism is dependent on the friction loss inside the draw bar mechanism. This problem has not been well addressed in previous works.

This paper reports the analysis and test results of a motorized high-speed spindle for machining centers, developed in the National Chung Cheng University. As reported in our previous work [20], thermally-induced bearing load of this developed spindle is managed by an active bearing load control mechanism and other design measures. The emphases of this paper are put on the centrifugal-force-induced characteristic variations of the shaft/bearing and draw bar mechanism performance at dynamic state.

2 Spindle layout

Figure 1 is the layout of a high-speed spindle with 20 000 rpm/14 kw developed in the National Chung Cheng University. The dmN value of the spindle is approximated to 1.65 million (in the case of steel ball bearing) or 2 million (in case of ceramic ball bearing). The preload is initially set by a spring preload mechanism. An optional active bearing load monitoring and control mechanism [20] consisting of the piezoelectric actuators and strain-gauge load sensors is used to on-line adjust the bearing loading according the cutting conditions. Thermally-induced bearing load is managed by the sliding bushes, the water cooling, and oil-air lubrication.

Although an AC induction motor is used for this spindle, it is worth to point out here that permanent magnet motors has a better potential to simultaneously meet the high speed, high power, and high shaft natural frequency requirements. A high-speed high-power spindle will ask for high shaft natural frequency. A high natural frequency means that large shaft diameter and short bearing spacing between front and rear bearings are a necessity. Because the motor power is determined by the rotor cross section, a rotor with large OD and short length is preferred to meet the high shaft natural frequency requirement while with a satisfied high motor power. In such a case, the spindle speed, however, will be limited by the allowable maximum circumferential speed of the rotor OD. On the other hand, to push the spindle speed to an extremely high level while still with a satisfied high motor power, a small OD and large length rotor is preferred. This measure, however, will set a limit to the shaft natural frequency. Therefore, it is difficult to design an AC induction motor spindle to simultaneously meet the high speed, high power, and high shaft natural frequency requirements.

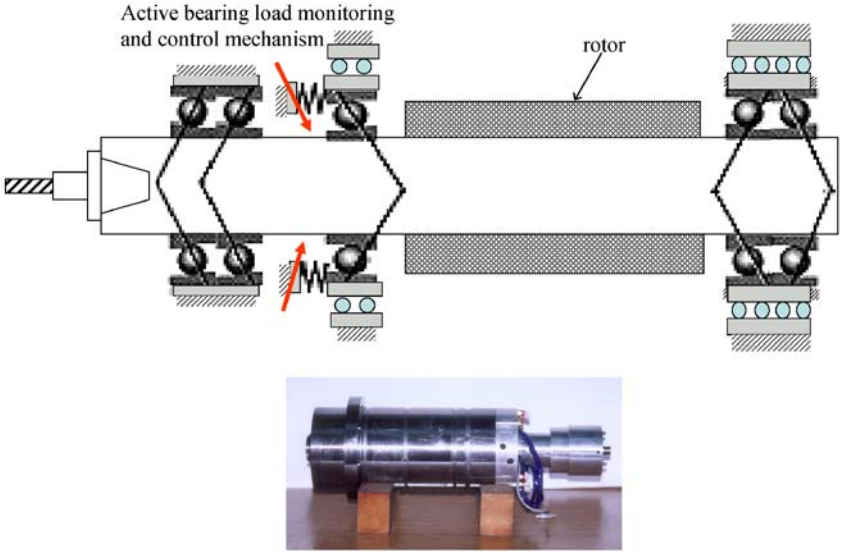

Fig. 1 Bearing/shaft layout of the developed high-speed spindle

Permanent magnet motors appear to have a better max. circumferential speed than the AC induction motor [3]. Permanent magnet motors also have lower inertia and lower heat. Therefore, in the trend to pursue a high-speed, high-power, and high-shaft-natural-frequency spindle, permanent magnet motors will be a better candidate than the AC induction motor.

3 Model and analysis of the shaft/bearing system

The rigid rotor dynamic configuration of the high speed spindle is shown in Fig. 2. Using the Largrange's approach, the rotor dynamics of the spindle was formulated as:

$$\begin{bmatrix} m & 0 & 0 & 0 \\ 0 & m & 0 & 0 \\ 0 & 0 & I_d & 0 \\ 0 & 0 & 0 & I_d \end{bmatrix} \begin{Bmatrix} \ddot{x} \\ \ddot{y} \\ \ddot{\alpha} \\ \ddot{\beta} \end{Bmatrix} + \begin{bmatrix} 0 & 0 & 0 & 0 \\ 0 & 0 & 0 & 0 \\ 0 & 0 & 0 & \omega I_p \\ 0 & 0 & -\omega I_p & 0 \end{bmatrix} \times \begin{Bmatrix} \dot{x} \\ \dot{y} \\ \dot{\alpha} \\ \dot{\beta} \end{Bmatrix} + \begin{bmatrix} k_3 & 0 & 0 & -k_5 \\ 0 & k_3 & k_5 & 0 \\ 0 & k_5 & k_4 & 0 \\ -k_5 & 0 & 0 & k_4 \end{bmatrix} \begin{Bmatrix} x \\ y \\ \alpha \\ \beta \end{Bmatrix} = \begin{Bmatrix} F_x \\ F_y \\ -LF_y \\ LF_x \end{Bmatrix} \quad (1)$$

where

$$k_3 = 3k_1 + 2k_2$$
$$k_4 = k_1\left(L_1^2 + L_2^2 + L_3^2\right) + k_2\left(L_4^2 + L_5^2\right)$$
$$k_5 = -k_1(L_1 + L_2 + L_3) + k_2(L_4 + L_5)$$

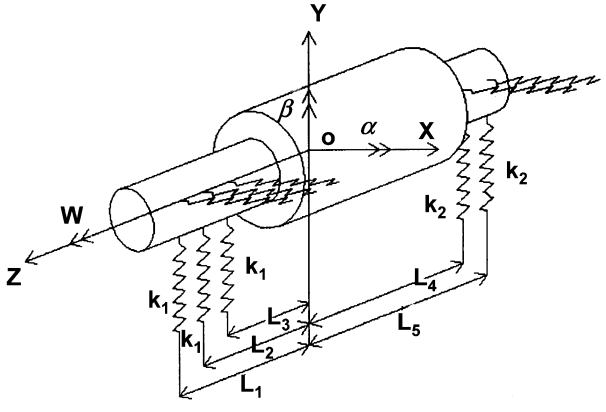

Fig. 2 Rotor dynamic model of the spindle

L: the length from the tooltip to the shaft mass center.

Table 1 lists the parameters of the developed spindle. Values in Table 1 are measured relative to the mass center CG. The rotor dynamic analysis result of the spindle is plotted in Fig. 3. It was found that the gyroscopic effect of the spindle shaft is not significantly because the whirl modes are not changed significantly with the spindle speed up to 250 000 rpm. As a rule of thumb, the first natural frequency must be about twice the maximum operating speed of the spindle. The first critical speed of the developed spindle was identified as around 66 567 rpm.

Table 1 Rotor dynamic parameters of the high speed spindle

Parameters	Values	Parameters	Values(m)
m	15.447(kg)	L_1	0.119
I_d	0.248 (kgm^2)	L_2	0.168
I_p	0.011845 (kgm^2)	L_3	0.129
k_1	25×10^7(N/m)	L_4	−0.135
k_2	17×10^7(N/m)	L_5	−0.161
C.G. (mass center)	0.239(m)		

4 Model and analysis of the nonlinear bearing stiffness

In the previous analysis result, the bearing stiffness is assumed as a value at the static state. In this section, the nonlinear stiffness characteristics of the bearing at dynamic state will be considered. Centrifugal-force-induced bearing softening comes from two reasons. The first reason is centrifugal force of the running ball will result in a reduction of the contact load at the inner/raceway interface. Because the Hertz-contact stiffness is proportional to the contact load, the bearing stiffness will be decreased at the dynamic state. The bearing stiffness is a series stiffness combination of the ball/inner-raceway contact load and ball/outer-raceway contact load. That is:

$$k_{rj} = \frac{1}{\frac{1}{k_{rij}} + \frac{1}{k_{roj}}} \tag{2}$$

where

k_{rij} the radial stiffness at the ball/inner-raceway interface of the jth ball
k_{roj} the radial stiffness at the ball/outer-raceway interface of the jth ball
k_{rj} the overall radial stiffness of the jth ball.

At stationary state, the Hertz-contact loads at these two contact interfaces are equal. Because two series combined springs with equal stiffness will yield the maximum combined stiffness, the maximum bearing stiffness happens at the static state. At dynamical state, the centrifugal force of the running ball is added to the contact load at the ball/outer-raceway. At the same time, the centrifugal force also results in a reduction of the contact load at the ball/inner-raceway. Because the Hertz-contact stiffness is proportional to the contact load, the k_{roj} is increased while the k_{rij} is decreased with the spindle speed. Therefore, the series combined stiffness k_{rj} is continuously reduced with the spindle speed.

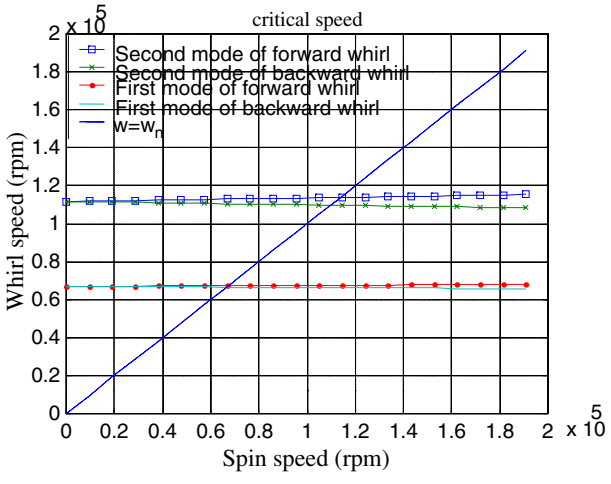

Fig. 3 Rotor dynamic analysis result of the spindle

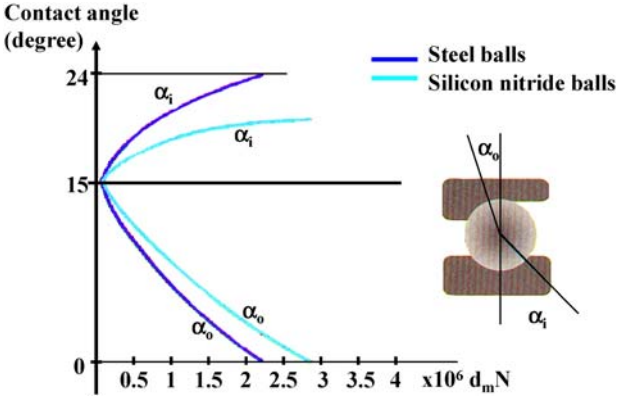

Fig. 4 The variations of the contact angles due to the centrifugal force (redraw from the SNFA catalog)

The second reason of the bearing softening is due to the increased contact angle of the ball/inner-raceway at the dynamic state. As shown in Fig. 4, when the bearings are at standstill (without rotation), the contact angles between the ball and the inner/outer raceways are identical. When the bearing begins to rotate, the inner and outer contact angles become dissimilar due to the centrifugal force and gyroscopic moment related to the bearing rotation, and bearing contact load changes. Increased contact angle of the inner raceway results in a reduction in the bearing stiffness. The main advantage of the lower density of ceramics is to reduce the centrifugal loading and variation of contact angle at the ball/inner-raceway.

To make a quantitative analysis of the dynamical bearing stiffness, the k_{roj} and k_{rij} must be known first. We follow the same symbols, definitions, procedures, and formulation as presented in chapter nine of the book by the Harris [21]. The centrifugal-force-induced bearing loads and contact angle change at high speed can be calculated from:

$$F_a - \sum_{j=1}^{j=Z} \left(\frac{K_{ij}\left(A_{1j} - X_{1j}\right)\delta_{ij}^{1.5} - \frac{\lambda_{ij} M_{gyj}}{D}\left(A_{2j} - X_{2j}\right)}{(f_i - 0.5)D + \delta_{ij}} \right) = 0 \tag{3}$$

$$F_r - \sum_{j=1}^{j=Z} \left(\frac{K_{ij}\left(A_{2j} - X_{2j}\right)\delta_{ij}^{1.5} - \frac{\lambda_{ij} M_{gyj}}{D}\left(A_{1j} - X_{1j}\right)}{(f_i - 0.5)D + \delta_{ij}} \right) \cos\psi_j = 0 \tag{4}$$

$$M - \sum_{j=1}^{j=Z} \left[\left(\frac{K_{ij}\left(A_{1j} - X_{1j}\right)\delta_{ij}^{1.5} - \frac{\lambda_{ij} M_{gyj}}{D}\left(A_{2j} - X_{2j}\right)}{(f_i - 0.5)D + \delta_{ij}} \right) R_i + \frac{\lambda_{ij} M_{gyj}}{D} r_i \right] \cos\psi_j = 0 \tag{5}$$

Definitions of all symbols in Eqs. (3–5) can be found from the book [21]. Because these three equations are

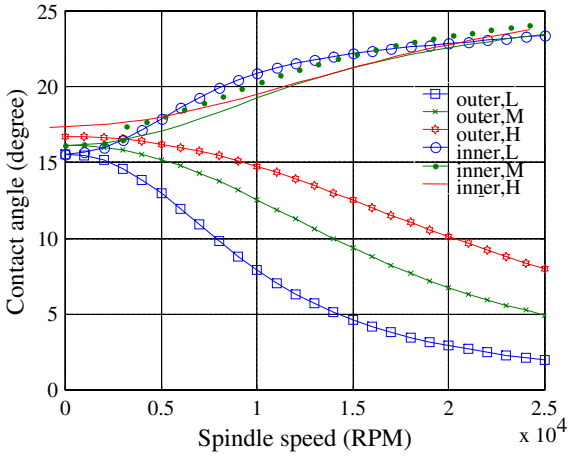

Fig. 5 Contact angle at the dynamic state

highly coupled and nonlinear, a Newton–Raphson numerical method was used to solve the three equations. Figures 5 and 6 are the simulation results of the contact angle change and contact load change of the bearing at dynamic state for the case of a FAG HS7013 bearing. In the simulation result, three preload levels, light (L), medium (M), and heavy (H) as specified in the FAG bearing catalog, are used.

After the contact load and contact angle changes at dynamic states are solved from Eqs. (3–5), the Hertz contact stiffness of the ball can be calculated as:

$$k_{ij} = 1.5K_{ij}\delta_{ij}^{0.5}$$
$$k_{oj} = 1.5K_{oj}\delta_{oj}^{0.5} \tag{6}$$

where

δ_{ij} the contact load at the inner raceway of the jth ball

δ_{oj} the contact load at the outer raceway of the jth ball

K_{ij} and K_{oj} the parameters that depend on the bearing geometry and materials.

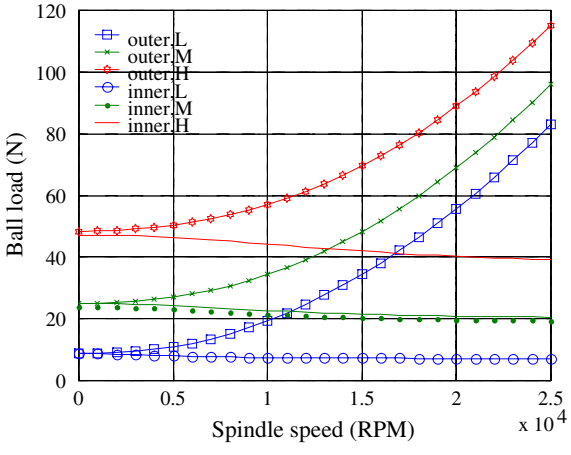

Fig. 6 Contact loads at dynamic state

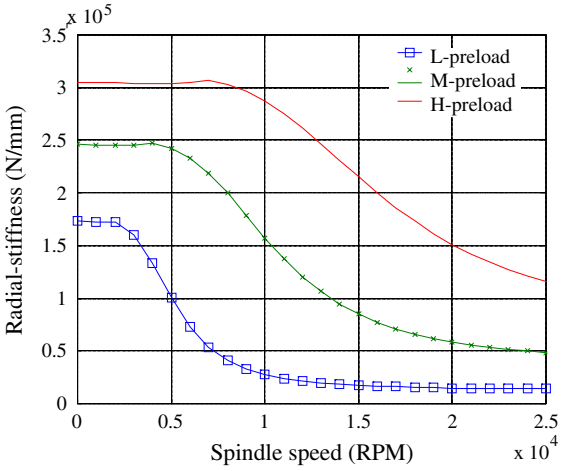

Fig. 7 Radial stiffness at dynamic state

The radial stiffness of the ball contact stiffness in the inner and outer raceways can be calculated from the triangular geometry relationship. That is:

$$k_{rij} = \left(1.5K_{ij}\delta_{ij}^{0.5}\right)\cos\alpha_{ij}$$
$$k_{roj} = \left(1.5K_{oj}\delta_{oj}^{0.5}\right)\cos\alpha_{oj} \tag{7}$$

where

α_{ij} the contact angle at the inner raceway of the jth ball

αoj the contact angle at the outer raceway of the jth ball.

Because the radial stiffness in Eq. (7) is in the local coordinate, the combined radial stiffness of every ball in the whole bearing in the global coordinate system can be formulated using the virtual work principle. That is:

$$K_r = \frac{1}{\frac{1}{J[k_\tau]J^T} + \frac{1}{P\cot\alpha_n/(\delta_a - \delta_{a0})}} \tag{8}$$

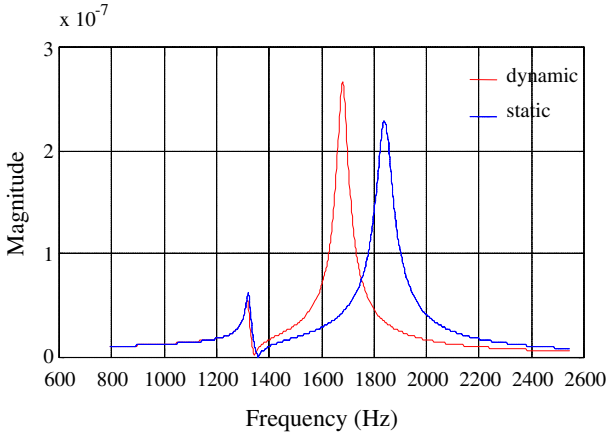

Fig. 8 Frequency response of the spindle at the static and dynamic states

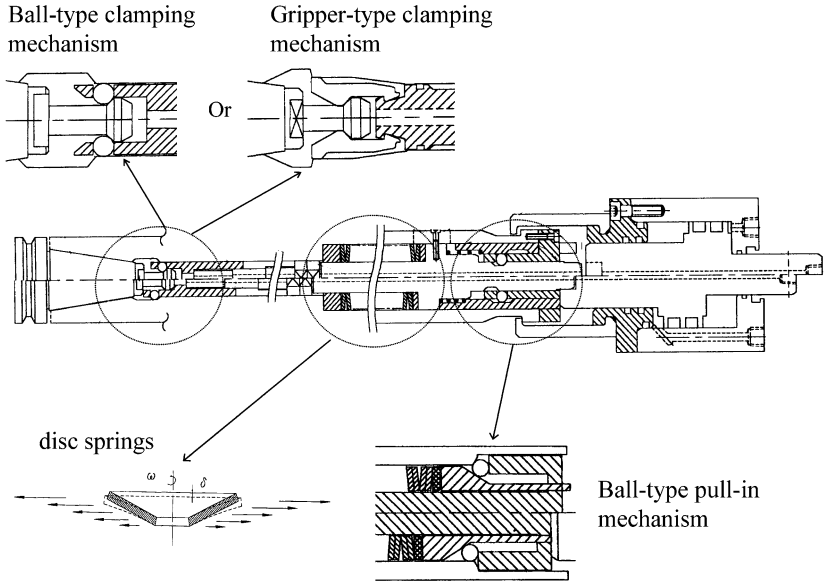

Fig. 9 The draw bar mechanism

$$J = [\cos\psi_1 \quad \cos\psi_2 \quad \cdots \quad \cos\psi_n]_{1\times n} \tag{9}$$

$$[k_\tau] = \begin{bmatrix} k_{r1} & & & \\ & k_{r2} & & \\ & & \ddots & \\ & & & k_{rZ} \end{bmatrix}_{Z\times Z} \tag{10}$$

where

ψ_j the angular position of the jth ball in the global corrdinate
P the initial preload of the bearing
δ_{a0} the initial axial displacement at the static state
δ_a the axial displacement at the dynamic state.

Figure 7 is the simulation result of the bearing radial stiffness at dynamic state. Finally, Fig. 8 shows the change of the frequency response function of the spindle at the dynamic state.

5 Model and analysis draw-bar mechanism

Figure 9 shows the draw bar mechanism of the developed high-speed spindle. Draw force exerted on the toolholder/spindle interface is produced by the stacked disc springs inside the draw bar mechanism. Pull-in force from the compressed disc springs is amplified by a ball-type pull-in mechanism. The pull-in force is transmitted to the clamping unit consisting of another ball-type or gripper-type clamping mechanism. By carefully selecting geometric parameters, the final draw force exerted on the toolholder/spindle interface is about triple that of the disc spring force. One problem of the conventional draw bar mechanism is that the disc spring and force amplification mechanism are designed based on the static load analysis. The influence of the centrifugal force at high speed on the draw bar mechanism is not clear.

5.1 Disc spring

Because of the centrifugal force, a deformation will be observed on the disc spring at high rotating speed and

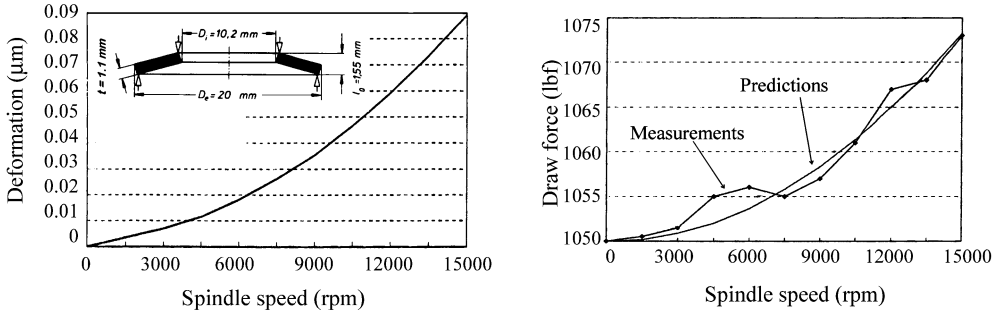

Fig. 10 Draw forces at dynamic state

a Deformation of disc spring

b Variation of draw force

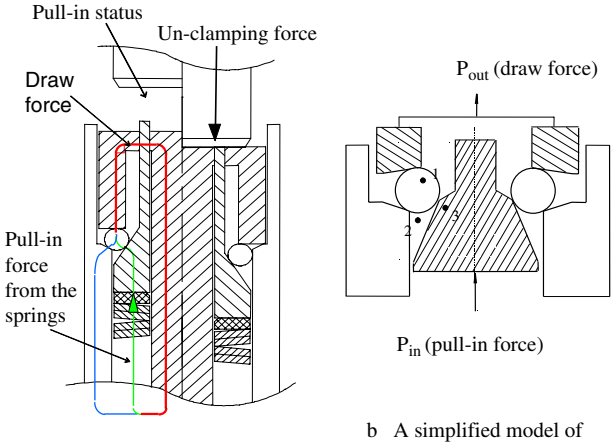

a Pull-in Mechanism

b A simplified model of the pull-in mechanism

Fig. 11 Ball-type pull-in mechanism

consequently reduce the spring force. An analytical model [18] based on the Hamilton's principle had been developed to predict the centrifugal-force induced deformation of the disc spring as shown in Fig. 10(a). Through analysis and experimental verification, it was found that the force reduction is not significant (see Fig. 10(b)). Spring force reduction due to the centrifugal-force is less than 5% of the total spring force at a speed up to 15,000 rpm.

5.2 Force amplification mechanism

As mentioned before, the ball-type pull-in mechanism can amplify the disc spring force by proper geometric parameters designed at the static state. In practice, the centrifugal force of the ball at high speed will add another force on the final draw force. Therefore, it is necessary to predict and control the additional centrifugal force. A ball-type pull-in mechanism is shown in Fig. 11(a). At the pull-in status, the spring force is amplified through the contact geometry of the steel ball. A simplified model is shown in Fig. 11(b). The input force is the spring force and the output is the draw force.

Geometrical parameters of the contacted ball of the pull-in mechanism are defined in Fig. 12(a). Free body diagram of the steel ball is depicted in Fig. 12(b). Friction of the ball contact interface is assigned as μ_k. At static state, the force and moment equivalent conditions must be satisfied as:

$$\sum F_x = 0 \Rightarrow F_3 \cdot \sin(\alpha+\beta) + u_k F_3 \cdot \cos(\alpha+\beta) + u_k F_1 \cdot \sin(\theta-\beta) - F_1 \cos(\theta-\beta) + f_2 = 0 \tag{11}$$

$$\sum F_y = 0 \Rightarrow \mathrm{F}_2 = F_3 \cdot \cos(\alpha+\beta) - u_k F_3 \cdot \sin(\alpha+\beta) - F_1 \cdot \sin(\theta-\beta) - u_k F \cdot \cos(\theta-\beta) \tag{12}$$

$$\sum M_0 = 0 \Rightarrow f_2 = u_k \cdot (F_3 - F_1) \tag{13}$$

$$P_{in} = F_1 \cdot [\sin\theta + u_k \cos\theta] \tag{14}$$

$$P_{out} = F_3 \cdot [\cos\alpha - u_k \sin\alpha] \tag{15}$$

Solving the Eqs. (11–15) simultaneously, we can obtain the following results:

$$\lambda \equiv \frac{P_{out}}{P_{in}} = \frac{\cos(\alpha+\phi)}{\sin(\theta+\phi)} \cdot \frac{\cos(\theta-\beta+\phi)+u_k/r}{\sin(\alpha+\beta+\phi)+u_k/r} \tag{16}$$

$$F_1 = \frac{P_{in}}{r \cdot \sin(\theta+\phi)} \tag{17}$$

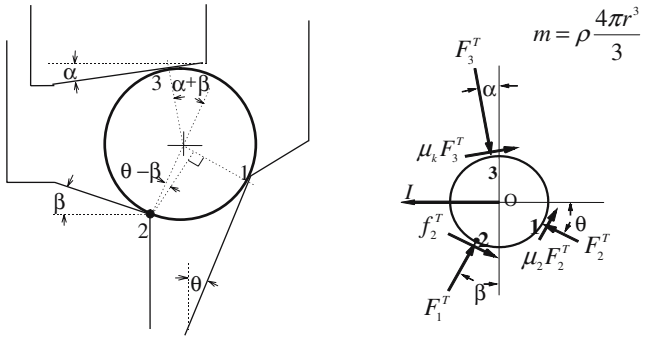

a Geometric parameters of the ball-type mechanism

b Free-body diagram of the steel ball

Fig. 12 The geometric parameters and the free-body diagram of the steel-ball

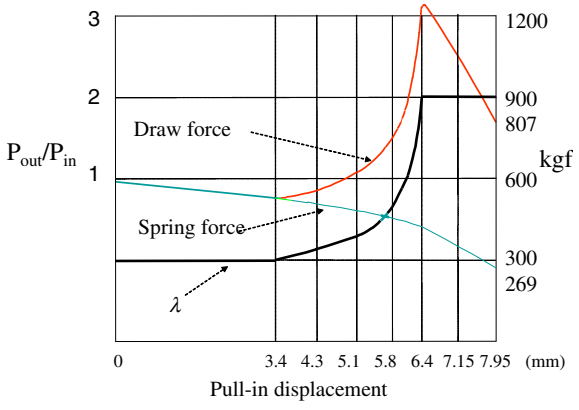

Fig. 13 Mechanical efficiency at the static state

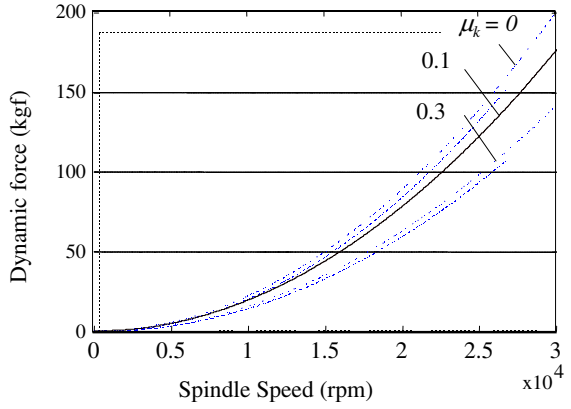

Fig. 14 Dynamic draw force

$$F_2 = P_{in} \cdot \left[\frac{\cos(\alpha+\beta+\phi) \cdot [\cos(\theta-\beta+\phi)+u_k/r]}{\sin(\theta+\phi) \cdot [\sin(\alpha+\beta+\phi)+u_k/r]} - \frac{\sin(\theta-\beta+\phi)}{\sin(\theta+\phi)} \right] \quad (18)$$

$$f_2 = P_{in} \cdot \left[\frac{u_k/r \cdot [\cos(\theta-\beta+\phi)+u_k/r]}{\sin(\theta+\phi) \cdot [\sin(\alpha+\beta+\phi)+u_k/r]} - \frac{u_k/r}{\sin(\theta+\phi)} \right] \quad (19)$$

$$F_3 = P_{in} \cdot \left[\frac{\cos(\theta-\beta+\phi)+u_k/r}{\sin(\theta+\phi) \cdot [r \cdot \sin(\alpha+\beta+\phi)+u_k]} \right] \quad (20)$$

where $\phi = \tan^{-1} u_k$, $r = \sqrt{1+u_k^2}$.

The λ in Eq. (16) is defined as the mechanical efficiency of the ball-type pull-in mechanism. The mechanical efficiency can be determined by selecting a set of proper geometric parameters in Eq. (16). Figure 13 shows an example of the mechanical efficiency, spring force, and draw force as a function of the displacement of the pull-in process at static case. A draw force triple that of the spring force is gained from the designed mechanical efficiency.

At the dynamic state, if the centrifugal force of the steel ball must be taken into account (as shown in the Fig. 12 (b)), the dynamic draw force can be formulated through the same procedures and becomes:

$$P_{out}^T = \lambda \cdot P_{in}^T + \frac{\cos\beta \cdot \cos(\alpha+\phi)}{\sin(\alpha+\beta+\phi)+u_k/r} \cdot I. \quad (21)$$

where $I=mR\omega^2$ is the centrifugal force of the steel ball. Notice that the centrifugal force will be a plus to the draw force in this case. However, depending on the geometric parameters, the centrifugal force is possible to be a minus to the draw force. Figure 14 shows the simulation result of the centrifugal force effect at different friction coefficient values. The increased dynamic draw force due to the centrifugal force of the steel ball is dependent on the friction coefficients. At a spindle speed up to 25 000 rpm, a dynamic force about 150–200 kgf is added to the static draw force.

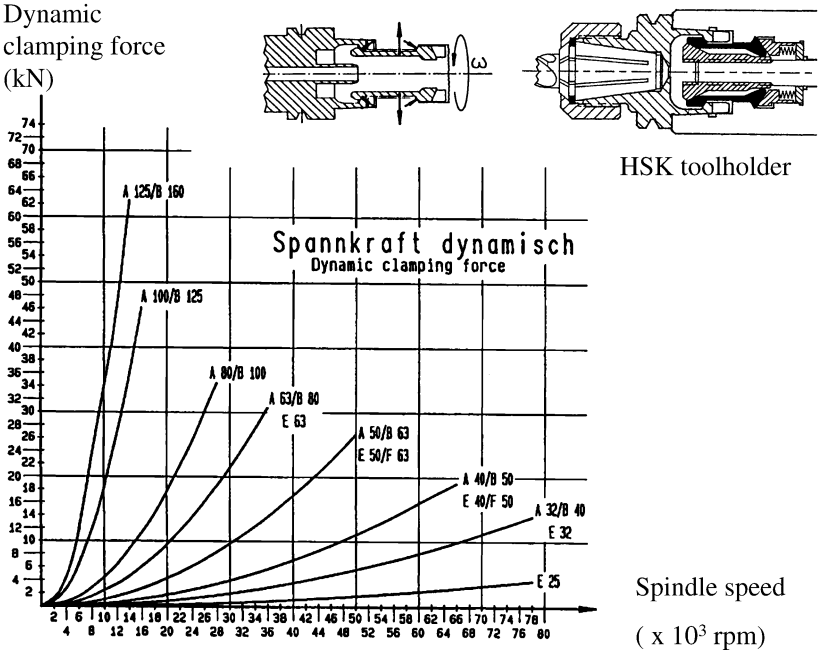

Fig. 15 Dynamic force of the wedge type gripper [22]

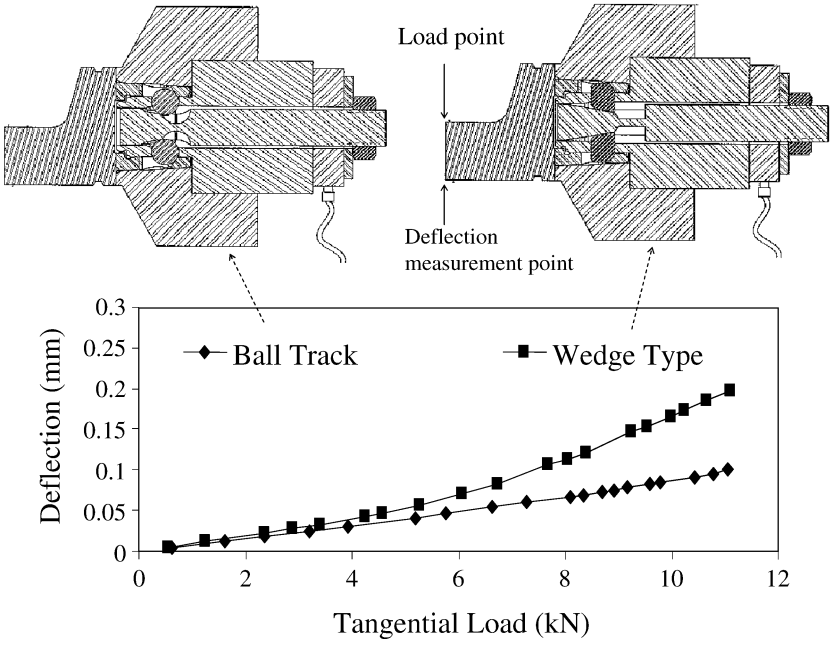

Fig. 16 Stiffness comparisons of wedge type and ball track mechanisms [23]

Notice that the dynamic force is decreased when the friction coefficient is increased. The friction influence is especially important to the hollow type HSK toolholder if the gripper is used to clamp the toolholder. Figure 15 shows the dynamic force of a HSK holder [22] that is calculated without the consideration of the friction influence. Because the wedge gripper has much large friction than the ball-type clamping mechanism, the reduction of the dynamic force due to the gripper friction can not be ignored. Kennametal Inc. made an experimental test to compare the stiffness of the face/tapper contact interface using the ball track and wedge type mechanisms, as shown in Fig. 16. Both mechanisms have the same mechanical amplification of 3:1 designed at the static state. However, the experimental test result has shown that the ball-type mechanism outperforms the wedge type mechanism. It is believed that since the theoretical mechanical advantages were the same for both mechanisms, the wedge type mechanism must have had greater frictional losses. If the dynamic force is involved, the stiffness difference between these two mechanisms will be enlarged due to the friction loss influence.

6 Conclusions

It was proved that at high speeds, centrifugal force can play an important role in spindle dynamics. Shaft/bearing stiffness as well as the natural frequency decreased at high speeds. Bearing softening due to the centrifugal force is the dominant source to the reduced spindle stiffness at high speeds, while the gyroscopic effect is considered as the secondary source. Contact stiffness reduction and contact angle change of the ball/inner-raceway is the major reason to the bearing softening at high speeds.

The toolholder/spindle interface stiffness is strongly determined by the draw force of the draw bar mechanism. Analysis results show that the dynamic draw force at high speeds is significantly different from that designed at the static state. Softening of the disc spring due to the centrifugal force can result in a reduction of the draw force. However, the reduction is not significant. Centrifugal force of the steel ball of the ball-type pull-in and clamp mechanisms can contribute a significant plus to the mechanical efficiency of the draw bar mechanism at dynamic state. The mechanical efficiency, however, is dependent on the friction inside the draw bar mechanism. Mechanical efficiency of the draw bar mechanism is reduced with increased friction. Because of the low friction coefficient, the ball-type mechanism is superior to the wedge type mechanism.

References

1. Weck M, Koch A (1993) Spindle-bearing systems for high-speed applications in machine tools. Ann CIRP 42:1
2. Schulz H (1992) High-speed machining. Ann CIRP 41:2
3. Voll H, Ramer P, Schulz H, Schall D (1999) On the way to a new generation of spindles. Proc 1999 Sino-German Joint Symposium on High-Speed and High Precision Machining, 15–16 March 1999, pp 45–53
4. Tsutsumi M, Chung IS, Murakami Y, Ito Y (1985) Dynamic characteristics of spindle-bearing system in machine tools. Bulletin of JSME 28(244):2460–2466
5. Al-Shareef KJH, Bradon JA (1990) On the effects of variations in the design parameters on the dynamic performance of machine tool spindle-bearing system. Int J Mach Tool Manuf 30:431–445
6. Weck M, Hennes N, Krell M (1999) Spindle and toolsystems with high damping. Ann CIRP 48(1):297–302
7. Smith S, Jacobs TP, Halley J (1999) The effect of drawbar force on metal removal rate in milling. Ann CIRP 48(1):293–296
8. Weck M, Schubert I (1994) New interface machine/tool: hollow shank. Ann CIRP 43(1):345–348

9. Agapiou J, Rivin E, Xie C (1995) Toolholder/spindle interfaces for CNC machine tools. Ann CIRP 44(1):383–387
10. Tlusty J, Livingston R, Teng YB (1986) Nonlinearites in spindle bearings and their effect. Ann CIRP 35(1):269–273
11. Soon MP, Stone BJ (1998) The stiffness of stability indeterminate spindle systems with nonlinear bearings. Int J Adv Manuf Technol 14:787–794
12. Shin YC (1992) Bearing nonlinearity and stability analysis in high speed machining. Trans ASME J Eng Ind 114:23–30
13. Stein JL, Tu JF (1996) A state-space model for monitoring thermally induced preload in anti-friction spindle bearings of high-speed machine tools. Trans ASME J Dyn Syst Measure Control 116:372–386
14. Li H, Shin YC (2004) Analysis of bearing configuration effects on high speed spindles using an integrated dynamic thermo-mechanical spindle model. Int J Mach Tools Manuf 44:347–364
15. Lin C-W, Tu J, Kamman J (2003) An integrated thermo-mechanical-dynamic model to characterize machine tool spindles during very high speed rotation. Int J Mach Tools Manuf 43:1035–1050
16. Riven E (1993) Influence of toolholder interfaces on tooling performance. Trans NAMRI/SME 21:173–179
17. Aoyama T, Inasaki I (2001) Performances of HSK tool interfaces under high rotational speed. Ann CIRP 50(1):280–284
18. Lin CC (1999) The development of a high speed spindle for machining center. Technical Report, National Chung Cheng University, NSC grant No. 86-2622-E-194-001R
19. Smith S, Jacobs TP, Halley J (1999) The effect of drawbar force on metal removal rate in milling. Ann CIRP 48(1):293–296
20. Chen JS, Chen KW (in press) Bearing Load Analysis and Control of a Motorized High Speed Spindle. Int J Mach Tool Manuf
21. Harris TA (2001) Rolling bearing analysis. Wiley, New York
22. Sykora H (1997) Training for OTT-JAKOB power drawbar systems. OTT-JAKOB Spanntechnik
23. Erickson R (2001) Tooling and taper interface considertios for high speed machining. High Speed Machining Workshop, 6 Nov 2001